



HAL
open science

Combining DNA scaffolds and acoustic force spectroscopy to characterize individual protein bonds

Yong Jian Wang, Claire Valotteau, Adrien Aimard, Lorenzo Villanueva, Dorota Kostrz, Maryne Follenfant, Terence Strick, Patrick Chames, Felix Rico, Charlie Gosse, et al.

► To cite this version:

Yong Jian Wang, Claire Valotteau, Adrien Aimard, Lorenzo Villanueva, Dorota Kostrz, et al.. Combining DNA scaffolds and acoustic force spectroscopy to characterize individual protein bonds. *Biophysical Journal*, 2023, 122 (12), pp.2518-2530. 10.1016/j.bpj.2023.05.004 . hal-04165173

HAL Id: hal-04165173

<https://hal.science/hal-04165173>

Submitted on 18 Jul 2023

HAL is a multi-disciplinary open access archive for the deposit and dissemination of scientific research documents, whether they are published or not. The documents may come from teaching and research institutions in France or abroad, or from public or private research centers.

L'archive ouverte pluridisciplinaire **HAL**, est destinée au dépôt et à la diffusion de documents scientifiques de niveau recherche, publiés ou non, émanant des établissements d'enseignement et de recherche français ou étrangers, des laboratoires publics ou privés.

Article

Combining DNA scaffolds and acoustic force spectroscopy to characterize individual protein bonds

Yong Jian Wang^{1,*}, Claire Valotteau^{1,*}, Adrien Aimard², Lorenzo Villanueva¹, Dorota Kostrz³, Maryne Follenfant³, Terence Strick³, Patrick Chames², Felix Rico¹, Charlie Gosse³, and Laurent Limozin^{1,*}

¹Aix-Marseille Université, CNRS, INSERM, Laboratoire Adhesion et Inflammation, Turing Centre for Living systems, Marseille, France

²Aix-Marseille Université, CNRS, INSERM, Institut Paoli-Calmettes, Centre de Recherche en Cancerologie de Marseille, Marseille, France

³Institut de Biologie de l'Ecole Normale Supérieure, ENS, CNRS, INSERM, PSL Research University, Paris, France

*Correspondence: laurent.limozin@inserm.fr, yong-jian.wang@inserm.fr, claire.valotteau@inserm.fr

ABSTRACT Single-molecule data are of great significance in biology, chemistry, and medicine. However, new experimental tools to characterize, in a multiplexed manner, protein bond rupture under force are still needed. Acoustic force spectroscopy (AFS) is an emerging manipulation technique which generates acoustic waves to apply force in parallel on multiple microbeads tethered to a surface. We here exploit this configuration in combination with the recently developed modular junctioned-DNA (J-DNA) scaffold that have been designed to study protein-protein interactions at the single-molecule level. By applying repetitive constant force steps on the FKBP12-rapamycin-FRB complex, we measure its unbinding kinetics under force at the single-bond level. Special efforts are made in analyzing the data in order to identify potential pitfalls. We propose a calibration method allowing *in situ* force determination during the course of the unbinding measurement. We compare our results with well-established techniques, such as magnetic tweezers, to ensure their accuracy. We also apply our strategy to study the force dependent rupture of a single domain antibody with its antigen. Overall, we get a good agreement with the published parameters that have been obtained at zero force and population level. Thus, our technique offers single-molecule precision for multiplexed measurements of interactions of biotechnological and medical interest.

SIGNIFICANCE (MAX 120 WORDS)

As observed in various physiological contexts, mechanical constraints play a previously underestimated role on the properties and function of protein bonds. The characterization of such interactions requires single-molecule force spectroscopy approaches, **for which combining high precision and high throughput remain challenging.** The present work associates for the first time DNA scaffolds with acoustic force spectroscopy to measure the force response of individual biomolecular complexes. Parallel monitoring over time of single bond ruptures is achieved with simultaneous force calibration. This proof-of-principle is established for two protein bonds of biomedical interest, opening promising perspectives for biotechnological and medical studies. (97 words)

INTRODUCTION

Biomolecules binding properties are governing biological phenomena and, consequently, are relevant for evaluating therapeutics. While bulk measurements performed on populations of molecules remain the standard characterization techniques, single-molecule force spectroscopy (SMFS) on individual pairs of interacting partners has emerged as a powerful complementary strategy, because it uniquely gives access to individual bond response to force. This ability is particularly significant for the study of biological phenomena where mechanical forces intervene in bond function, like in hematology (1), neuroscience (2), immunology (3), or cell biology (4). In practice, the various SMFS tools (5) can be separated in two categories. On one hand, several techniques scrutinize a single bond at a time, the interacting molecules being mounted in series with a spring-like dynamometer such as in atomic force microscopy (AFM) (6, 7), optical tweezers (OT) (2, 8), or micropipette-based biomembrane force probe (9). Typically, a force ramp is applied to the bond and the force at the rupture is determined from the extension of the calibrated spring. The dependence of the off-rate as a function of the force is then deduced by a mathematical transformation of the rupture force distributions obtained at different loading rates (10). Offering a high precision, these methods however suffer from a limited throughput. On the other hand, measurements on several bonds at a time usually involve a spatially extended force field acting on microbeads, a configuration encountered in magnetic tweezers (MT) (11), laminar flow chamber (LFC) (12, 13), centrifugal force microscopy (CFM) (14, 15), dielectrophoretic force spectroscopy (DFS) (16), and more recently acoustic force spectroscopy (AFS) (17–19). In those techniques, the distribution of bond lifetimes can be directly measured at constant force. Of note, calibration of the force often relies on a physical model; it also usually assumes the homogeneity of the force field and of the bead properties (20, 21). These simplifications allow high throughput measurements but are not always flawless.

Whether investigating bonds one by one or in parallel, the stochastic nature of bond rupture requires the accumulation of a large number of events in order to characterize the unbinding distribution. This intrinsic constraint of single-molecule approaches is often experimentally problematic because protein bond characterization suffers from irreversible unbinding: the molecular partners are taken apart by force, preventing any rebinding and therefore limiting the accessible statistics. To address

this issue, molecular scaffolds that include a leash have been engineered to keep the reactants in close proximity despite the dissociation, hence favouring rebinding. An additional advantage provided by such constructs is mechanical fingerprinting: upon bond rupture, the two partners must end separated by the length of the leash; events that do not verify this criterion can be easily sorted out and discarded (1, 22–24). In practice, these leashes may consist in peptidic chains (1, 2, 4, 25, 26), single DNA strands (27–29), or double DNA strands, with (15, 22, 30) or without nicks (20, 31, 32). While peptidic linkers require to design and produce a specific fusion protein, nucleic acids based structures offer more modularity when combined with state-of-the-art DNA-protein coupling strategies (20, 23, 33–38). As a matter of fact, the latter kind of scaffold has already been used for non-covalent bond characterization on various SMFS setups: OT (22, 27–29), MT (20, 28, 31, 32), CFM (14, 15), and LFC (30).

Here, we introduce the combination of a modular DNA scaffold, namely junctured-DNA (J-DNA) (20, 39), with AFS, an emerging parallel method which potentially offers a large dynamic range of fast force application (17, 18) (Fig. 1). The probed protein complex is attached to both the surface of the flow cell and a bead via kilobase pair-long DNA shanks (Fig. S1A). The force applied can thus be calibrated independently for each protein complex using the inverted pendulum method commonly used in MT experiment (40, 41) (Fig. S2), with the notable advantage of a direct and accurate determination of the tether length. Indeed, contrarily to what has been experimentally demonstrated for MT (42–44), AFS does not impose the orientation of the bead upon pulling and this way facilitates the determination of the point of attachment of the DNA on the bead (Fig. S1B). Additionally, while individual fit of calibration parameters (bead diffusion coefficient and pendulum stiffness) can be hampered by the acquisition conditions (camera frame rate) for higher forces, a global fit performed for all applied powers for each bead allows to overcome this issue. All in all, simultaneous calibration and unbinding measurements are achieved for all forces, within the limit imposed by the precision of the bead position determination and the equipartition theorem. This ability to determine the applied force during an unbinding experiment is critical because the acoustic field is known to exhibit high chip-to-chip variability and high spatial heterogeneity (18, 45, 46).

We first apply our method to the FKBP12-rapamycin-FRB complex, a well-known system that has been studied using numerous biochemical (47–49) and biophysical (50–55) techniques, including SMFS (20, 25). In addition to its interest for benchmarking (20, 56), rapamycin has an important biomedical relevance, being one of the earliest modulator of protein-protein interaction to have reached the clinic (57, 58). Our results successfully compare with the unbinding data obtained by surface plasmon resonance (SPR) (50, 51) and by SMFS (20, 25). Furthermore, the determination of the off-rate vs force dependence for different individual pairs of interacting molecules provides a check of the method accuracy, and a way to look for bond heterogeneity.

For a second proof-of-concept, we turn to a model antigen-antibody bond involving a nanobody, a class of compounds which exhibit remarkable binding properties (59). More specifically, those 12 kDa antibodies serve as building blocks for bispecific constructs used for cancer immunotherapy (60) and in this context, the bonds they form are subjected to mechanical forces (13). Hence, it fully justifies to characterize such an interaction under an applied load. With an off-rate at zero force in

the range of 10^4 s, an extended force range helped to achieve off-rate determination of such a strong bond in a reduced time. Doing so, the off-rate extrapolated at zero force is found in good agreement with independent determination relying on SPR (61).

MATERIALS AND METHODS

Molecules and reagents

Proteins. All proteins were labeled with a single azido group so as to enable their conjugation via click chemistry to 5' DBCO-modified oligonucleotides, the latter 9-base pair long sequences being used for further site-specific ligation to the J-DNA scaffolds (20). More precisely, for the study of the rapamycin complex, a 4-azido-L-phenylalanine residue was introduced at the N-terminus of both FKBP12 and FRB proteins by unnatural amino acid incorporation (62–64), which yielded the previously characterized FKBP12_{M0AzF} and FRB_{A2020AzF} mutants (20). For the nanobody-antigen study, SdAb19 (later noted Nef19), a nanobody directed against the HIV-1 Nef protein (61), was C-terminally fused to both a c-myc tag and a hexa-his one, produced in the periplasm of *E. coli*, and purified by immobilized metal affinity purification as previously described (65). In parallel, a truncated portion (aa. 57-205) of HIV-1 Nef was produced in the cytoplasm of *E. Coli* and purified as above. Finally, microbial transglutaminase (Zedira, Darmstadt, Germany) and its substrate azido-PEG₃-amine (Click Chemistry Tools, Scottsdale, AZ, USA) were used to site specifically add an azide function on the glutamine residue of the c-myc tag of both proteins (66, 67).

J-DNA scaffolds. Similarly to the others nucleic acids-based scaffolds recently developed for single-molecule investigations (15, 16, 20, 22, 27–32, 39), J-DNAs have a forceps-like anatomy (23) (Fig. S1A). The interacting protein partners are engrafted at the tips of this nanotool and the handles allowing the manipulation (i.e. the bead and the glass surface) are attached to the extremities of the shanks. The leash, which prevents the whole assembly to be torn apart upon unbinding, connects the two tip-shank segments at the junctions. We here relied on our previous protocol (20) to synthesize two versions of the J-DNAs and functionalized them with the proteins of interest that had been tagged with single-azido group (20). More specifically, in the present study we used both the asymmetric scaffold described in Kostrz et al. (20) and a new symmetric one (Table S1). In the latter construct the length of the shanks was modified so as to make it easier to discriminate protein-protein interactions from protein-surface ones, i.e. to have extension jumps of different amplitudes for specific protein-protein binding and for non-specific sticking to the bead or to the chamber (Table S2, Fig. S1C). Transforming the asymmetric scaffold into the symmetric one was simply achieved by shifting the positions on the template of the primers used in the first PCR reaction of the J-DNA fabrication process (see the caption of Table S1 for the sequences).

Beads. Streptavidin-coated silica beads of 1.58 μm in diameter (1.0% w/v, Spherotech, Lake forest, IL, USA, cat. SVSIP-15-5) were used for the FKBP12-rapamycin-FRB measurements. For the Nef-Nef19 ones, we additionally relied on 3 μm diameter beads (1.0% w/v, Spherotech, cat. SVSIP-30-5).

Buffers. Unless otherwise specified, all chemicals for buffer preparation were from Sigma-Aldrich (Merck, Darmstadt, Germany). Functionalization buffer was prepared using phosphate buffer saline (PBS), bovine serum albumin (BSA, cat. A7030), and Pluronic F-127 (cat. 9003-11-6). Single use aliquots of rapamycin (cat. 53123-88-9) were prepared by dissolution of the powder in dimethylsulfoxide (DMSO) to a concentration of 50 μM and stored at -80°C . Importantly, due to its instability, this compound was always added extemporaneously to the working buffer. All the solutions were supplemented with 5 mM sodium azide and 0.5 mM ethylenediaminetetraacetic acid (EDTA), filtered at 0.2 μm , and stored at 4°C . Assays with J-DNA functionalized with FKBP12 and FRB were conducted in mTOR buffer: 20 mM potassium HEPES pH 7.8, 100 mM KCl, 5 mM MgCl_2 , 0.1% Tween-20, 0.5 mg/ml BSA, and 2 mM dithiothreitol (DTT), supplemented with 500 nM rapamycin. Assays with J-DNA functionalized with Nef and Nef19 were conducted in PBS, 0.1% Tween-20, and 0.5 mg/ml BSA.

AFS chamber preparation

The AFS chamber (Lumicks, Amsterdam, Netherlands) consists of two parallel glass slides delineating a 100 μm high fluid channel of area approximately $10 \times 2 \text{ mm}^2$. The internal chamber volume with tubing is about 20 μL . A transparent piezoelectric element is present on top of the assembly to generate the acoustic waves that pull on the beads (Fig. 1A). A syringe connected to the outlet port allows one to suck solutions placed in the inlet reservoir, either manually or with a syringe pump (Aladdin 1000; WPI, Sarasota, FL, USA).

The AFS chamber surface was silanized to obtain a highly hydrophobic surface in order to facilitate further binding of antibodies. To this end, it was first incubated with a piranha solution (2/3 sulfuric acid + 1/3 hydrogen peroxide 50% in water) (12) for 10 min, rinsed with water, dried with nitrogen, incubated with Sigmacote® (Sigma-Aldrich, cat. SL2) for 1 min, dried, rinsed with acetone (Sigma) and rinsed with PBS. The AFS chamber was next functionalized with polyclonal anti-digoxigenin from sheep (Sigma, Roche, cat. 11333089001) by injection of 50 μL of a solution at 200 $\mu\text{g}/\text{mL}$ (20 min incubation). The AFS chamber was finally double-passivated by flushing first 200 μL of 0.2% PBS-BSA (30 min incubation) and then 200 μL of 0.5% PBS-Pluronic solution (30 min incubation).

For the measurements on the FKBP12-rapamycin-FRB complex, the AFS chamber was rinsed with 200 μL of mTOR buffer; then the J-DNAs on which the proteins had been pre-assembled were injected at a 0.5 to 1 pM concentration in mTOR buffer (30 min incubation). Anchoring of the scaffold to the anti-digoxigenin glass surface is mediated by digoxigenin molecules located at one extremity of one of the shanks (Fig. S1A). Streptavidin-coated beads were washed two times by spinning down 10 μL of solution at 0.5 % w/v diluted in 1 mL of mTOR buffer. After a final resuspension in 50 μL of mTOR buffer supplemented with 500 nM of rapamycin, the particles were injected in the AFS chamber and allowed to settle for few minutes so that they can bind to the extremity of the second shank, which is decorated with biotin molecules (Fig. S1A). A gentle flow of rapamycin containing mTOR buffer was then applied to remove the untethered beads. **All FKBP12-rapamycin-FRB data presented were obtained on the same AFS chip, 2 different injected samples, and 4 different fields of view (FOV) (beads ID1-5:**

sample 1 FOV 1; beads ID6-13: sample 1 FOV 2; beads ID14-19: sample 1 FOV 3; beads ID20-21: sample 2).

For the measurements of Nef-Nef19, the AFS chamber was only passivated by injection of 0.2 mL of 0.2 % BSA in PBS (60 min incubation). The prefucionalized J-DNAs diluted at 1pM in the same buffer were then injected in the AFS chamber (30 min incubation) and another rinsing with 0.2 mL PBS-BSA were realized. Beads were washed three times by spinning down 50 μ L of solution at 1% w/v diluted in 1 mL of 0.2% BSA in PBS. After a final resuspension in 50 μ L of 0.2 % BSA in PBS, they were injected in the AFS chamber and incubated for few minutes. A gentle flow of 0.2 % BSA in PBS was finally applied to remove the untethered beads. **All Nef-Nef19 data presented were obtained on the same AFS chip, 6 different injected samples and each bead in different FOV; all beads were 1.58 μ m in diameter except beads ID5-7 which were 3 μ m in diameter.**

Microscope and AFS setup

The sample is illuminated by a fiber-coupled LED (M660F1, Thorlabs, Newton, NJ, USA) and imaged using an inverted microscope (IX71, Olympus, Rungis, France) equipped with a 20 \times air objective (Uplan F, Olympus) and an USB-camera (UI1324, IDS, Obersulm, Germany) capable of acquiring frames of 1936 \times 1216 pixels at 55 Hz, which corresponds to a 458 \times 420 μ m² field of view. Higher frame rates can be achieved for smaller areas. The AFS chamber is screwed on a sample holder which vertical position can be adjusted by a nanometer step motor (M-110.12S, PI, Karlsruhe, Germany) driven by a digital controller.

The piezo on top of the AFS chamber is driven by a function generator (Lumicks, generation 3) controlled by a computer (via USB) and an interface written in LABVIEW (National Instruments, Austin, TX, USA). The application to the piezo of an alternative tension in the MHz frequency range creates a stationary acoustic pressure field in the chamber: two nodes are typically located at 25 μ m and 75 μ m altitude in the 100 μ m high fluidic channel (Fig. 1A) (17). Starting from a value pre-calibrated by the manufacturer for each AFS chamber, the driving frequency was adjusted manually in order to reach the so-called resonance frequency (RF) for which the vertical pressure gradient is maximized at the vicinity of the chamber floor. In case of force drop due to RF drift, for example caused by a minute temperature change, the frequency was slightly readjusted by the user in order to increase the force before starting a new measurement run. The amplifier setting is called *power* by the manufacturer and is expressed in % units. In order to favor implementation of our findings by other users, we have decided to keep both appellation and unit. It is further said by the manufacturer that the set value scales linearly with the force applied to a bead at a given altitude (18).

The temperature inside the chamber is regulated to 25 °C by an integrated proportional derivative controller, a sensor being placed in the middle of the flow cell and two heating elements warming up the whole fluidic channel. Using the embedded thermometer, the measured variation of the temperature inside the chamber are less than 0.2 °C for low to moderate power (i.e. for 0 to 30% power).

Measurement protocol and data acquisition

The setup is controlled through the LABVIEW software provided by the manufacturer (Lumicks v1.4.0), which we have modified for our needs. More precisely, we have added an option to generate periodic acoustic force patterns corresponding to tunable steps of power P and duration T . For example, in a typical unbinding experiment, a 0 % power step of typical duration $T^A \geq 5$ min is used to determine the anchor point of each bead. Next, a cycle alternating a very low power ($P^L < 0.01\%$) step and test power step (power P) is repeated typically 100 times. The corresponding durations T^L and T need to be adapted to the nature of interacting partners, and can vary from a fraction of a minute up to 15 min. As a rule of thumb, T is set as, at least, 2 or 3 times the inverse of the expected off-rate.

The AFS software also allows one to track each bead on the fly and in 3D thanks to real-time image analysis. On a standard desktop computer, up to 100 beads can be tracked at 55 Hz. The x,y -position corresponds to the center of the bead diffraction pattern while the z -position is determined using a predefined look-up-table (LUT) ranging from 0 to 10 000 nm in 100 nm steps (41). Importantly, whereas the coordinates in the horizontal plane are absolute, the one along the vertical axis is only relative. The individual bead traces are recorded in a tdms file (i.e. LABVIEW format) together with the power amplitude, chip driving frequency, and temperature.

Data analysis

The data analysis is performed in two phases: a) during phases 1-6 described below, one single tdms file is analyzed. It contains cycling force data at a single test power for multiple tethered beads from a single field of view; b) during phases 7-8, the outcome of the first part of the process for various measurements at different test powers is merged for each individual bead. Global fitting procedures are then performed and synthesis plots are produced.

1. **Initialization.** The tdms file contains the bead traces (x,y,z -coordinates vs time) acquired from one field of view during one cyclic measurement. One or several test traces are selected for analysis as well as several reference traces (if available). So-called test traces are typically obtained from beads tethered via a single functional J-DNA. Reference traces are typically obtained from beads directly stuck onto the surface, exhibiting minimal fluctuations and allowing to correct for drift of the chamber position over time. The time interval for the analysis of all traces is also set.

The following phases 2-6 are applied for each test trace.

2. **Baseline correction and precision on bead position determination.** This operation compensates for apparent drift of the sample due to lateral and vertical motions, caused for example by the dilatation of the microscope elements under temperature variations of the environment. The correction is performed in 3 directions by calculating an average reference trace mimicking the motion of the whole sample and withdrawing it from the test trace. If several reference traces are available, the average reference trace is calculated as the mean for each coordinate, followed by a rolling average over typically 100 s, which largely cancels the noise in reference localization but which is sufficient to correct for sample slow motions. If no surface-bound bead

is available for reference, a self-reference can be performed on a J-DNA tethered bead. The self-reference trace is built taking as a basis the coordinates from the test bead as follows: the z -position of the test bead is selected at low power, while the x and y positions of the test bead are selected at high power. The rest of the trace is obtained by interpolating by a constant value in order to fill in the gaps at high power for z and low power for x, y . The complete self-reference trace is obtained after a rolling average on a time window of *ca.* 15 min, in order to completely smooth out the effect of interpolation between cycles. On a fully immobile bead we measured a standard deviation $SD(x) = 15$ nm in the horizontal motion and $SD(z) = 20$ nm in the vertical motion. Conversely, for a tethered bead under a few pN force, $SD(x) = 25$ nm and $SD(z) = 50$ nm.

3. Anchor point determination. One here relies on the data acquired during the dedicated time interval T^A or on all time points obtained at power P^L . The anchor point coordinates (x_A, y_A, z_A) are obtained, in the horizontal plane, as the time average of x and y and, along the vertical axis, as the minimal value of z after a rolling average on *ca.* 10 s (Fig. S3C). This duration was chosen in order to smooth the z signal without augmenting the minimal measured altitude. It corresponds to a plateau in the curve the minimal altitude vs size of the averaging window. In case the bead is not exploring the whole available space, for example due to transient binding to the surface, the center of the envelope of the x, y -positions is used instead of the in-plane barycenter (Fig. S3B). For this, a kernel density estimation of the x, y -coordinates distribution is performed, defining typically 20 contour lines, and the center of the external contour is taken for setting (x_A, y_A) .

4. Tether length and pulling angle determination. The length L of the scaffold corresponds to the distance between its point of attachment to the bead, A' , and the point of anchoring to the surface, A (Figs. S2 and S3). Noting x, y, z the coordinates of the point B of lowest altitude at the surface of the bead, one has:

$$L = \left((x - x_A)^2 + (y - y_A)^2 + (z + R - z_A)^2 \right)^{1/2} - R \quad (1)$$

where R is the radius of the bead. Combining localization errors in 3 directions, one estimates the precision on L determination to be around 100 nm. The pulling direction was determined by calculating the polar angle θ (Fig. S3):

$$\theta = \arcsin \left(\left((x - x_A)^2 + (y - y_A)^2 \right)^{1/2} / (L + R) \right) \quad (2)$$

5. Opening events detection. This operation is performed on the $Z = z - z_A$ trace, separately on each time interval during which the power is applied. A 1D gaussian filter of window size 1 s is first applied and the signal is normalized between 0 and 1. This duration is chosen in order to reduce noise while keeping the accuracy of on dwell time duration. The crossings of a 0.5 threshold value are recorded and the step size is determined following the original procedure found in github.com/thomasbkahn/step-detect. If no step is detected, the average altitude Z is compared with the middle altitude representing equidistance between the open and closed states plateau, typically $Z^* = 900$ nm. If $Z > Z^*$, one considers that the J-DNA did not close back at the previous low power interval (no-close event). If $Z < Z^*$, one considers that the J-DNA did not open during the test power interval. The lifetime of the close state is measured between the onset of high power application plus a delay and the opening

time. The delay accounts for the time it takes to effectively apply the force on the bond, which is largely set by the duration of bead uplift and empirically estimated to be 1 s maximum.

6. Power spectrum calculation. The single sided power spectrum density (PSD) of the bead fluctuation signal is calculated separately on $x - x_A$ and $y - y_A$ thanks to the signal.periodogram routine from the PYTHON Scipy package. In a default mode that is used for the "force calibration on the fly", we take into account all the points tagged as belonging to the open state. Alternatively, in the independent calibration mode, a specific time interval can be selected, for which phases 1-4 are performed as above and phase 5 is skipped. This mode can also be used to calculate the PSD using data obtained at a high frame rate and specifically dedicated for calibration of large forces. For graphical representation, PSD are binned on an equally spaced log frequency scale.

7. PSD fitting and force calibration. For a 55 Hz acquisition frame-rate, we typically work with frequency f ranging from 0.1 to 15 Hz. For a given bead, the PSD along x at power P_i is compared with:

$$PSD_i^x(f) = \sum_{n=0}^1 \frac{4(k_B T)^2}{D_i^x (k_i^x)^2} \frac{1}{1 + ((f + n f_s)/f_{ci}^x)^2} \frac{\sin^2(\pi \tau_e (f + n f_s))}{(\pi \tau_e (f + n f_s))^2} \quad (3)$$

where D_i^x is the bead diffusion coefficient parallel to the surface, k_i^x the stiffness of the pendulum, and $f_{ci}^x = D_i^x k_i^x / (2\pi k_B T)$ the corner frequency which delineates the elastic and viscous parts of the spectrum obtained at power P_i . $k_B T$ is the thermal energy at temperature T . **We have introduced the correction for blur and aliasing, noting f_s the sampling frequency and τ_e the exposure time (68, 69). The sum was restricted to $n=0, 1$ corresponding to the two most significant terms for the single-sided Fourier spectrum. Typical values are $f_s = 50$ Hz, $\tau_e = 9$ ms, or $f_s = 500$ Hz, $\tau_e = 1$ ms., depending on the bead ID.** Writing Z_i the bead height from the chamber surface at power P_i and R^x the bead radius, the diffusion coefficient can be approximated by (70):

$$D_i^x = \frac{k_B T}{6\pi \nu R^x} \left[1 - \frac{9}{16} \frac{R^x}{Z_i + R^x} + \frac{1}{8} \left(\frac{R^x}{Z_i + R^x} \right)^3 \right]^{-1} \quad (4)$$

where ν is the dynamic viscosity of water. A global fit using Eq. 3 and Eq. 4 is then applied to all PSD_i^x simultaneously, taking the k_i^x and R^x as fitting parameters. This global fitting allows calibration of one bead-scaffold pair at all forces without requiring to have $f_{max}/2 > f_c$ for all spectra. Therefore, we can perform calibration at standard acquisition frame rate which is adapted for long lifetime measurements and multiplexed beads tracking. Alternatively, individual PSD fits can also be performed applying Eq. 3 and taking D_i^x and k_i^x as fitting parameters. This is possible when the condition $f_{ci}^x < f_{max}/2$ is fulfilled, i.e. for low power or high acquisition frequency. In this case, however, the maximal measurable spring constant would be $k_{max} = f_{max} \pi k_B T / D \simeq 0.003$ pN/nm, taking $D = 0.2 \mu\text{m}^2/\text{s}$ from Fig. S6. Of note, from the equipartition theorem (see Fig. S2), the precision on the horizontal position determination sets a maximal measurable stiffness of $k'_{max} = k_B T / SD(x)^2 = 0.02$ pN/nm if we use $SD(x)=15$ nm the standard deviation mentioned above.

The force determined along x for a given bead at power P_i is given by:

$$F_i^x = k_i^x(L_i + R^x) \quad (5)$$

where L_i is the scaffold extension in its open state. Taking into account the analyses one can perform in both x and y directions, the average vertical force and bead radius are simply calculated as : $F_i = (F_i^x + F_i^y)/2$ and $R = (R^x + R^y)/2$. The force applied along the J-DNA when pulling at angle θ is thus:

$$F^\theta = (1/2)(F^x + F^y) \cos \theta \quad (6)$$

8. Survival curves plotting and fitting. For a given bead and a given power, all the dwell-times before opening, Δt , are pooled. It also includes the no-open events to which we attribute T , i.e. the duration of application of the power, as dwell time. All those values are next sorted by increasing order so as to build a survival fraction S corresponding to the fraction of J-DNA still closed at time t . The survival curve is fitted with a monoexponential function as expected for this type of process; it appears on a semilog graph as a straight line with a slope equal to the bond off-rate. **The non-rupture events are taken into account and the fit range is adjusted accordingly, to avoid any bias due to right censoring.** The uncertainty on the off-rate is calculated as the difference of slope of the survival curves calculated either on the first 50 unbinding events that were collected or on the last 50 ones.

RESULTS

Principle of the coupling between DNA scaffolds and AFS

After the beads have been injected in the AFS chamber and allowed to settle for a few minutes, the application of a limited power (1%) permits to collect the non-tethered ones at the first pressure node along z , far out of focus, and to flow them away. One can thus select the beads that are tethered to the surface via J-DNA molecules or that are non-specifically stuck (Fig. 1A), so as to track them using the acquisition software (Fig. 1B). Additional sorting can be performed by eliminating the beads for which the recorded x,y -trace is strongly anisotropic, which is a typical feature of beads likely tethered via multiple J-DNAs. If available in the field of view, one or several beads showing no Brownian motion can be selected as reference beads to enable baseline drift correction. Recording of the look-up tables (LUT) that contain, for each bead, its diffraction pattern as a function of the defocusing, is then performed by applying a power of 1 % and moving the microscope stage in the z direction (17, 41).

In a typical measurement, the piezo is driven by a rectangular signal, the power being periodically switched between two values: one nearly equal to zero (<0.01 %) and one able to put the scaffold under tension (Fig. 1C). Starting at nearly zero force with the proteins dissociated, the bead is at low height (Fig. 1C) and it exhibits strong fluctuations (Fig. 1D, left part of height profile in grey): the molecular partners can easily access each other but one cannot distinguish when binding occurs, if it occurs.

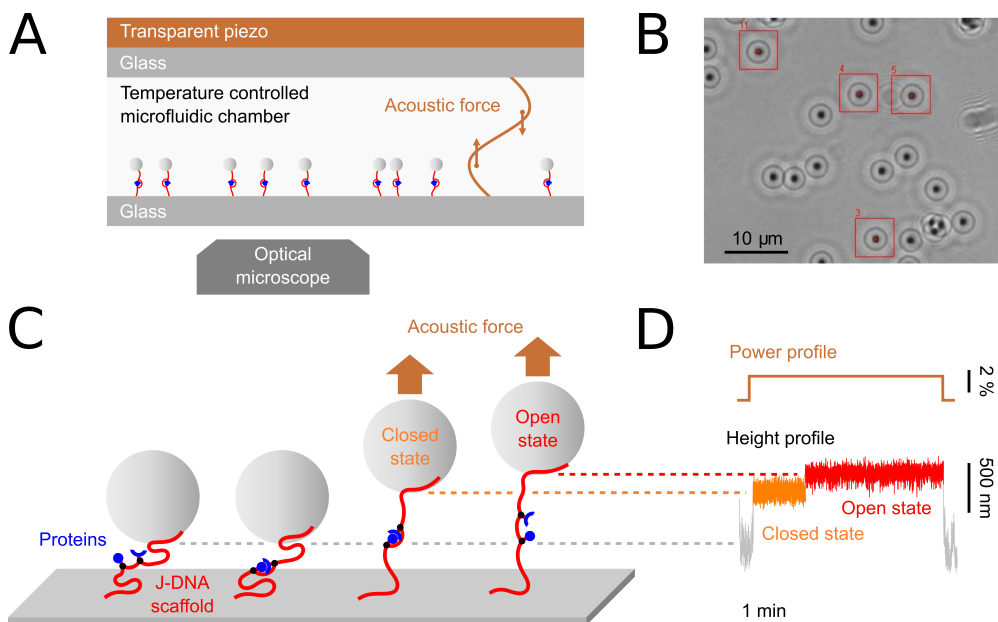


Figure 1: Principle of the method and sample trace. (A) Beads are tethered in a microfluidic chamber equipped with a piezo generating the acoustic waves and a temperature control system (Not to scale). (B) Part of the field of view showing beads that are selected (red squares) to be tracked in real-time and in 3D thanks to their diffraction fringes. (C) Each bead is tethered to the chamber surface through a J-DNA scaffold (red) maintaining the protein partners (blue) in close proximity via a leash. Bond formation occurs in absence of significant acoustic force. Upon application of an acoustic force, the difference in extension of the scaffold in the closed and in the open state allows one to distinguish the unbinding of the protein complex. (D) Corresponding power and height profile of the bead.

Upon application of a 2% test power, the bead height quickly increases to a plateau value and exhibits reduced fluctuations, corresponding to the closed state of the scaffold with the protein complex formed (Fig. 1D, orange trace). A sharp transition to a higher plateau is next observed, corresponding to the transition to the open state where the complex is dissociated (Fig. 1D, red trace). The difference between the two plateaus corresponds to approximately 200 nm, as expected from the length of the J-DNA leash (Table S2). The power is finally reduced, releasing the tension on the scaffold and permitting rebinding (Fig. 1D, right part of grey trace). Incidentally, for less than 5-20 % of the cycles, the bead directly reaches the highest plateau, meaning that no association occurred at low force (Fig.S16).

Once the x,y,z -traces are corrected from drift and the J-DNA anchor points at the chamber surface are determined, one proceeds to the analysis of the cycling force experiment *per se*. An example of z -trace obtained during 100 power cycles is shown on Fig. 2A with a zoom provided in Fig. 2B. An automatic step detection permits to : 1) measure the scaffold length extension upon jump Δz (see Fig. 2B); 2) distinguish the open and closed states on the trace at test power, as represented by the orange and red colors in Fig. 2A,B; 3) measure the duration Δt in closed state (bound complex) under application of high power (see Fig. 2B). The corresponding survival curve obtained from Δt is shown in Fig. 2C. The density distribution of Δz jumps is represented in Fig. 2D. The values are peaking between 200 nm and 300 nm, corresponding to the opening of the leash, as expected from Table S2. Similar plots acquired for other values of the power evidence a decrease of the bond lifetime

and an increase of jump amplitude with the applied force.

Measurement of the pulling angle

The pulling angle θ is the angle formed between the z -axis and the line passing by the anchor point and the bead center (see Fig. S3 for a geometrical depiction with the open J-DNA and Eq. 2 for the way this parameter is obtained from the measurements). As can be clearly seen in Fig. 2E for three representative beads, θ does not usually depend on the applied power. We also observed that in a same field of view its average value varies between 0 and 30° (Fig. S4). More strikingly, the pulling angle for a same bead may sometimes increase or decrease continuously by nearly 30° over the explored power range (see ID 1, 5 in Fig. S4). This illustrates the existence of lateral pressure nodes which orient the pulling axis and which positions can change with the applied power (45, 46).

Measurement of the scaffold length and of the applied force

The acoustic force applied to each bead is determined by calculating the power spectrum density (PSD) and relating it to the stiffness of an inverted pendulum having the length of the scaffold (40, 41), following Eq. 5 in the Materials and Methods section. We first examined the PSDs and the way to fit them.

PSD computation. The PSDs are computed from the bead lateral fluctuations for each test power. A typical example obtained in the x direction is presented on Fig. 2F. Traditionally, these data are obtained separately by applying a constant power for a given time. We propose here to extract these data directly from the applied force cycles (see Materials and Methods). This calibration "on the fly" avoids adding an additional calibration procedure. To show that this method provides the same results than an independent calibration, we performed both at the same test powers on the same scaffolds. Fig. S5 shows that the PSD are almost identical. The "on-the-fly" method provides a less noisy signal at low frequency since the signal has been accumulated over a longer time in total.

PSD fitting. We then propose to perform a global fit, using Eqs. 3 and 4, considering all the test powers for each bead, and determining a single bead radius for all powers and a value of stiffness k for each tested power. In order to validate this approach, **we have compared the diffusion coefficient D_i or the stiffness k_i obtained either from the global fit or from local fits (i.e. of individual PSDs when $f_c < f_{max}/2$). The two determinations match very well for k_i (Fig. S6A). In comparison, D_i values are more scattered on the plot (Fig. S6B) which could be due to the fact that this parameter is calculated for each power in individual fits, while a single parameter is used for all powers for the global fit.** This validates the global fit method, which allows to overcome some individual fit difficulties, for instance when the corner frequency cannot be pinpointed on the PSD because of the limited acquisition frequency. By combining "on the fly" calibration and global fit, we were able to compute and fit the PSDs for all beads at all test powers. The results for 21 beads tethered by J-DNA functionalized with the FKBP12 and FRB proteins are shown on Fig. S7 and Fig. S8 for the x and y -directions, respectively. The fits are superimposed

to the data, showing a good agreement for all powers. In addition, PSDs from 9 beads functionalized with the Nef and Nef19 are shown on Fig. S9, also showing a good fit quality.

Fitted bead radius. The distribution of R^x or R^y obtained for both molecular complexes fairly agrees with the nominal values and size distribution provided by the manufacturer, i.e. $0.78 \pm 0.12 \mu\text{m}$ and $1.48 \pm 0.32 \mu\text{m}$ for each bead type (Fig. S10). However, we systematically observed $R^x < R^y$, which we attributed to a poorer quality of the data and fit in the y -direction.

Fitted stiffness. Fig. S11 shows the fitted stiffnesses for different FKBP12-FRB scaffolds and powers. The stiffnesses measured in x or y directions exhibit very similar values. A non-linear dependence with the applied power is also noted, the curves being either concave or convex. This could be due to minute shift of the resonance frequency away or towards the driving frequency.

Length of J-DNA. The length of the J-DNA is measured between the anchor point at the chamber surface and the attachment point onto the bead, as illustrated by Fig. S3A (see Eq. 1 for its computation). First, one can here invoke some variation due to the random integration of digoxigenin and biotin at the extremities of the shanks. Using single labels would solve this issue but would also make J-DNA more prone to fully detach, which is unacceptable when performing day-long experiments. Second, the lengths we measure suggest limitations in the localization of the anchor point. More precisely, when working on dsDNA molecules with MT the latter operation is achieved with a high precision because one can supercoil the tether at low force so as to screw down the bead and have it landing on the anchor point (40). In our case such an approach is impossible because AFS cannot generate any torque, and because J-DNA cannot be supercoiled due to single bonds present at the junctures.

Force calculation. The force is then calculated following Eq. 5. Similarly to the stiffness, it depends non-linearly on the power (see Figs. 2G, S13). More specifically, the force typically varies from 0 to 20 pN as the power is increased. However, both the shape of the response and the maximum value one can achieve depends significantly on the position in the chamber, once more illustrating the existence of acoustic nodes in x and y (46). The variation with force of the length of open J-DNA is shown for the FKBP12-FRB scaffolds in Fig. S14. While, as expected, the length monotonously increases with applied force in most cases, some curves exhibit non-monotonic behaviour. This could stem from a limited precision in extended state determination due to errors in jump determination. Also, we did not succeed in satisfactorily adjusting the data to either the freely jointed chain model or to the worm-like chain one. In fact, to obtain a more accurate determination of the scaffold mechanical properties, dedicated investigations in the low force domain would be required, which are out of the scope of the present paper. Fig. S15 shows the difference of average scaffold extension between open and closed state as a function of force. The values are typically in the range 200-300 nm as expected from the molecular data in Table 1. The elastic stretching of the leash is also visible as a slight increase of the length with force.

Force dependence of the off-rate

The use of J-DNA allows repetitive measurements on individual bonds, cycling between the association of the proteins when the power is low and their dissociation when it is high (Fig. 1C and 2A).

The fraction of non-closed scaffolds observed when increasing P remains usually less than 0.2, indicating that the duration T^L the molecules spend at low force is sufficient for efficient rebinding (Fig. S16). It was also noticed that the cloud of points at low force exhibits a symmetric and homogeneous distribution around the anchor point (Fig. S3B), which we relate to a correct scaffold recoiling and thus more opportunities for the reactive partners to encounter.

At the test power, one measures the dwell time Δt , which corresponds to the time elapsed until an extension jump Δz is detected (Fig. 2B). The dwell times collected over the force cycles are used to generate a survival curve, which is established for each J-DNA and each applied force. **Since 100 cycles were applied and typically less than 20 of them did not show any bond formation (Fig. S16) between 75 and 100 rupture events per bead were collected at each force. Fig. S18 gives an overview of the number of forces measured per bead for the rapamycin system, which varies between 3 and 12 (7 in average).** These survival curves are individually fitted by a single mono-exponential function, yielding a straight line which slope is the off-rate when represented in semi-log scale (Fig. 2C and S17). Such off-rates k_{off} obtained for the FKBP12-rapamycin-FRB complex are next plotted as a function of applied force F for each scaffold. The k_{off} vs. F data for each scaffold were next fitted separately with the Bell model:

$$k_{\text{off}}(F) = k_{\text{off}}^0 \exp(x_b F / k_B T) \quad (7)$$

where k_{off}^0 is the off-rate in the absence of applied force and x_b is the distance from the potential well to the barrier on the interaction energy landscape (Fig. S18). Since the existence of lateral forces has been evidenced, to ensure that the influence of the pulling angle remains negligible we computed the force projected along the pulling angle (Eq. 6). The Bell parameters obtained considering these forces differ only marginally from the ones determined without projection of the force (see Fig. S18 for a comparison).

The Bell analyses performed on each of the 21 J-DNA functionalized with FKBP12 and FRB were superimposed (Fig. 3A, colored dots) and the corresponding k_{off}^0 and x_b fit values were reported on a unique graph (Fig. 3B). **Performing an average of the latter results with the inverse of the SDs as weight yielded $k_{\text{off}}^0 = 30 \pm 7 \times 10^{-3} \text{ s}^{-1}$ and $x_b = 0.34 \pm 0.32 \text{ nm}$ (Fig. 3B, black square).** Alternatively, all the off-rates determined on all 21 beads were pooled by force bins (Fig. 3A, black circles) and the obtained dataset was fitted using a single Bell plot, **taking into account the error bars. It gave $k_{\text{off}}^0 = 30 \pm 1 \times 10^{-3} \text{ s}^{-1}$ and $x_b = 0.37 \pm 0.03 \text{ nm}$ (Fig. 3B, black circle).** Therefore, the parameters provided by these two approaches are consistent. Furthermore, they agree with the ones retrieved with the same J-DNA mounted on magnetic tweezers: $k_{\text{off}}^0 = 30.5 \pm 0.2 \times 10^{-3} \text{ s}^{-1}$ and $x_b = 0.43 \pm 0.01 \text{ nm}$ (20) (Tables S3, S4 and Fig. 3B, green dashed-and-dotted lines). The off-rates extrapolated at zero force are also consistent with the determinations achieved by SPR, $20.5 \pm 1.5 \times 10^{-3} \text{ s}^{-1}$ (50) and $16.7 \pm 0.3 \times 10^{-3} \text{ s}^{-1}$ (51) (Tables S3 and Fig. 3B, red dashed lines), as well as by SMFS using another kind of scaffold, 26 and $32 \times 10^{-3} \text{ s}^{-1}$ (25) (Tables S3, S4 and Fig. 3B, green dashed-and-dotted line).

Additionally, Fig. 3 enables one to gain insight on individual behaviors. Despite the somehow profuse aspect of panel A,

measurements are in fact not excessively dispersed. First, the error bars on the pooled off-rate of panel A (black lines) typically represent a relative error of less than 50%. **As a consequence, the standard deviation for both k_{off}^0 and x_b corresponds to around 30 % of the mean, as represented for the black circle on panel B. However, parameters fitted for individual complex exhibit a much larger variation (colored points in panel B), which leads to large standard deviation for their weighted average (large error bars of the black square in panel B). Of note, the measurement error of off-rate per molecule can be visualized on Fig. S18 (typically set by the measurement of ca. 80-100 events), while Fig. 3A shows intermolecular heterogeneity. Each color dot on Fig. 3B relies on the observation of 250 to 1020 rupture events (see Tables S1 and S2 for detailed statistics).**

Similar measurements and analyses were performed for 9 J-DNA scaffolds functionalized with Nef and Nef19. This complex being much more long-lived than the FKBP12-rapamycin-FRB one, we aimed at applying higher forces to achieve unbinding with waiting times much shorter than $1/k_{\text{off}}^0 \simeq 10^4$ s. We used larger beads (3 μm diameter), in order to increase the acoustic force at equal power, without generating too much heat or shifting the resonance frequency too strongly. The force vs power data are represented on Fig S19: a sharp force increase can be observed when changing the diameter of the beads from 1.58 to 3 μm . However, as displayed on Fig. S20 survival curves, despite that force increase, the bond lifetime often exceeds the measurement time T . Thus, survival curves contain a limited number of rupture events and are censored at a maximal duration between 600 and 1200 s. While, due to this limitation, independent curve fit of off-rate vs force is not accurate, if even possible, due to lack of points (Fig. S21), one can perform a fit on pooled data, as shown on Fig. 4. **The Bell parameters are as follows: $k_{\text{off}}^0 = 0.18 \pm 0.1 \times 10^{-3} \text{ s}^{-1}$ and $x_b = 0.65 \pm 0.13 \text{ nm}$.** As for FKBP12-rapamycin-FRB, it agrees well with the $0.18 \times 10^{-3} \text{ s}^{-1}$ off-rate determined by SPR in the absence of force (61). Notice that x_b is almost doubled compared to the FKBP12-rapamycin-FRB case, while k_{off}^0 is reduced by a factor 10. Thus the Nef-Nef19 bond is much more stable at low force, but more sensitive to force.

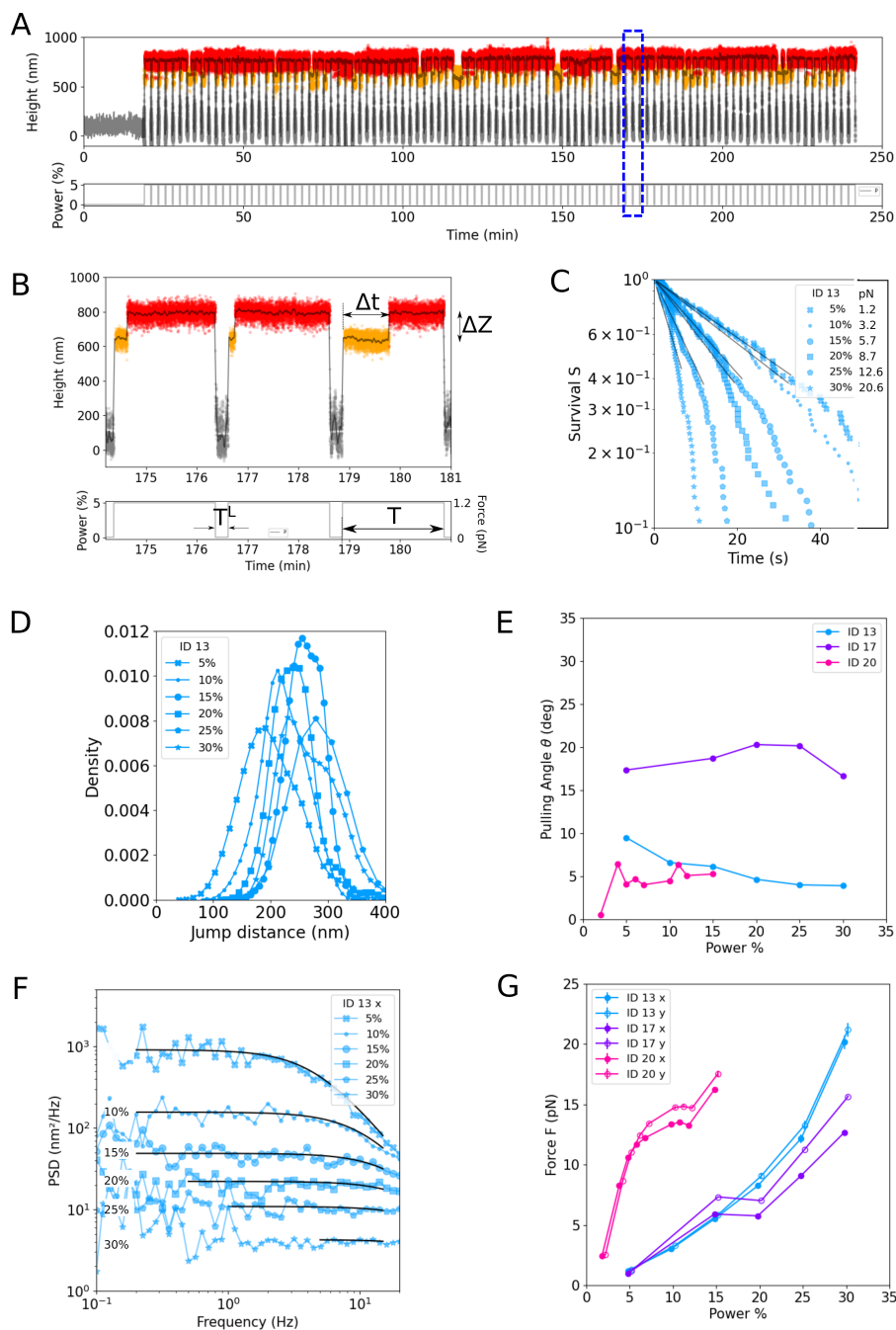


Figure 2: Tracking of a single bead under force cycles, bond lifetime determination, and force calibration. (A) Height trace Z obtained during 100 low/high power cycles. (B) Zoom of the trace in panel (A), indicated by the dashed blue rectangle. Based on power value and jump detection at high power, the trace is divided in 3 subsets: low power (grey), closed state at high power (orange), and open state at high power (red). Δt , which corresponds to the duration of the orange step, represents the dwell time before scaffold opening. ΔZ represents the height jump between the closed and the open state. **The applied force obtained after calibration is specified on the right axis.** (C) Survival curve calculated from the lifetime Δt distribution for one representative bead at different powers in %. Superimposed mono exponential fits : $S(\Delta t) = \exp(-\Delta t \cdot k_{\text{off}})$, with k_{off} the off-rate constant of the opening reaction. **The value of calibrated force for ID13 for each applied acoustic power is specified in the legend.** (D) Density kernel of jump distance ΔZ for the same bead as in panel (C) at different powers. (E) Pulling angle vs power for 3 representative beads. (F) x -power spectrum density for the same bead as in panel (D), at various applied powers P_i . Curves fits used to determine the bead radius R^x and the stiffnesses k_i^x are shown as black lines. (G) Force vs power for 3 representative beads, the same as in panel (E). Full symbols correspond to the results obtained from analyzing the bead Brownian motion along the x -direction and open symbols from the y -direction.

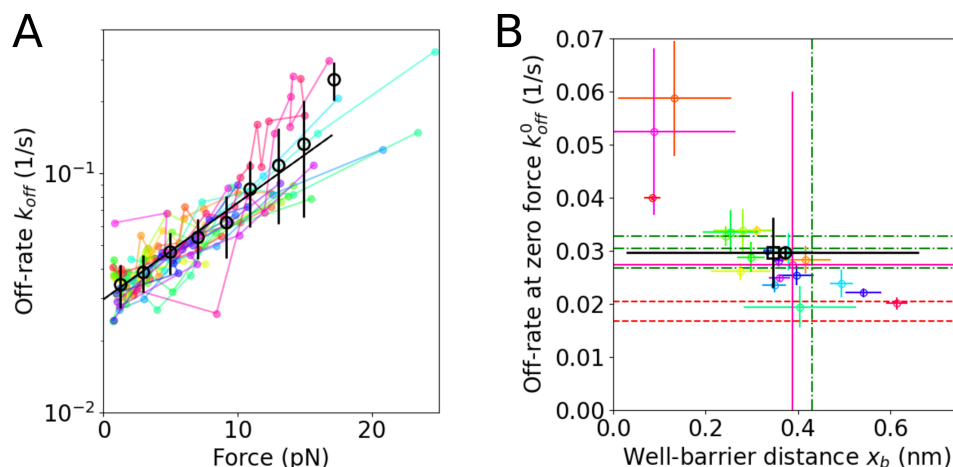


Figure 3: Bell plots for the FKBP12-rapamycin-FRB complex and corresponding fit. (A) The off-rate at different forces of individual molecules is shown in different colors. **The error bars on individual off-rate values are calculated as indicated in the Materials and Methods and, for the sake of clarity, they are omitted here and displayed in Fig. S18. The average values on force bins of equal size are shown as black circles, the vertical error bars showing the standard deviation of off-rate values in each force bin.** The dashed black line is the fit with Bell equation 7, taking into account the error bars. See Tables S1 and S2 for detailed statistics. (B) Off-rate in absence of applied force k_{off}^0 as a function of x_b , the distance from the potential well to the barrier on the energy landscape of the interaction, as obtained from the individual Bell fits shown in Fig. S18. **The same color code is used than in A to specify the different molecules measured. Each color dot relies on the observation of 250 to 1020 rupture events.** The error bars are the fitting errors when applying Bell model. The red dashed lines represent the values of off-rate measured by Surface Plasmon Resonance (50, 51). The green dashed-and-dotted lines were obtained using SMFS (20, 25). The black circle represent the parameter obtained from the global Bell fit represented as a black line in A (error bar = error on the fit). The black square represents the average of the colored points (error bar = SD).

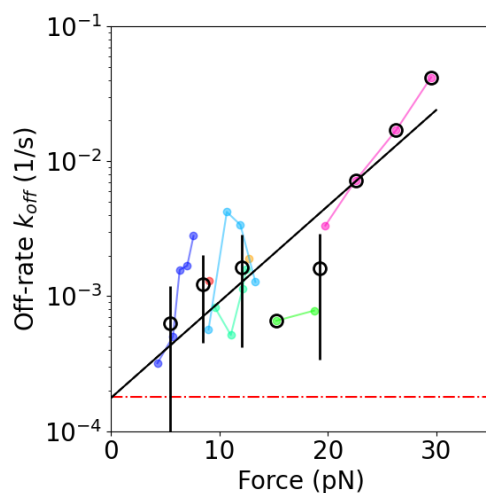


Figure 4: Bell plot for the Nef-Nef19 complex and corresponding fit. **The off-rate at different forces of individual molecules is shown in different colors.** The black circles correspond to the k_{off} averaged by equal force bins. The black line is the fit with Bell equation 7. The vertical error bars on the black points are calculated as the standard deviation of off-rate values in each force bin. The red horizontal dashed line represents the value of the off-rate measured by SPR (61).

DISCUSSION

Besides the now well-established MT (11, 40, 41) and LFC (12, 13), several new parallel SMFS techniques have recently appeared, for instance CFM (14, 15), DFS (16) and AFS (17–19). The latter method looks particularly promising because it has the potential to combine three attractive features: the possibility to monitor beads in parallel, an extended force range, and a fast actuation. A practical constraint of AFS lays in the current closed format of the commercial chambers, for which the development of surface regeneration procedures seems essential in order to guarantee the solidity and reproducibility of bead tethering. Next, as for other parallel methods like MT and LFC, a trade-off for the choice of bead size should be found to optimize the force range while limiting non-specific adhesion. A third drawback resides in the strong heterogeneity and the limited stability of the acoustic field, specially at high power where the sample may heat. One can propose to map the force field in a preliminary experiment and rely on the collected information to perform subsequent investigations; however, this would require perfect control of the external conditions (and notably of the chamber positioning). In fact, it is better to realize force calibration for each scrutinized protein complex. J-DNAs offer this opportunity because they are both scaffolds on which the molecular partners can be engrafted and tethers that can be used for force determination by the inverted pendulum method. Force calibration measurements are here achieved by collecting the corresponding data “on the fly”, during the investigations on bond rupture, and fitting them globally for each J-DNA. Hence, it allows maximum benefit to be derived from data acquired under standard experimental conditions at regular acquisition frequency. The accuracy of the force calibration is mainly associated with the precision in the determination of the bead position. Based on the maximal measurable stiffness $k_{max} = 0.003$ pN/nm, the maximal measurable force is $F_{max} = k_{max}(L + R) \simeq 35$ pN with a tether length $L \simeq 1\mu\text{m}$ and a bead radius $R \simeq 0.8\mu\text{m}$. Interestingly, such *in situ* calibration is hard to enforce with MT for instance, the orientation imposed to the bead by the magnets impeding accurate length measurement for DNAs only several kilobase pair-long. Some have proposed to add rulers or force sensors to overcome this difficulty (21, 44); still, in our case it would excessively complicate scaffold synthesis and would also restrain the range of explored forces. On the same line, we have thought of harnessing the amplitude of the height jump as an intrinsic reporter of the applied force but this observable did not yield convincing results (Fig. 2D).

The present work constructively combines AFS and J-DNA to study the response to force of single biomolecular bonds with individual calibration of the applied force. Utilizing a scaffold enables to observe enough dissociation events on the same two protein partners so that one can probe bond aging, a phenomenon we have not observed so far: the off-rate calculated either during the first 50 cycles of a measurement or during the last 50 ones are essentially identical (Fig. S22). It also enables to extract the individual Bell’s parameters for individual protein complexes. As a consequence, one can now compare the different complexes and challenge the concept of bond heterogeneity, as formalized by Raible et al. (71). Interestingly, among all possible environmental causes of heterogeneity (71), our setup removes the variable attachment of proteins to surface and non-specific interactions. **These advantages in hand, our observations show directly a dispersion of the Bell parameters k_{off}^0 and x_B for the FKBP12-rapamycin-FRB complex. The deviations of some of the survival curves from a monoexponential**

decay (ID5, ID13 in Fig. S17), point towards the interplay between phenomena taking place at multiple time scales, in line with previous reports (9, 72). The absence of such deviation for other molecules (ID11, ID12) may in fact be an additional manifestation of intermolecular heterogeneity. In contrast with our measurements, absence of heterogeneity has been recently measured for some protein unfolding (73). We remark also that the absence of bond heterogeneity may not question the concept of roughness of the energy landscape (74–76). Finally, a recent study demonstrated the potential of kinetic measurements on populations of single bonds in order to discriminate molecular mixtures, like polyclonal antibody samples (77): our method should also be very well suited for such an application.

Examination of Fig. 3B shows a negative correlation between k_{off}^0 and x_b for the FKBP12-rapamycin-FRB complex. To assess where this trend could originate from, we first hypothesized some relation with the properties of the experimental system (78). However, we observe no or limited correlation between x_b and parameters such as the bead radius (Fig. S23A) or the J-DNA length (Fig. S23B). We also calculated the correlation between the maximal force and the distance to the barrier, finding again no correlation (Fig. S23C). Additionally, we computed the effect of a parabolic potential imposed by the spring-like scaffold, as proposed by Friddle et al. (79), and found that the quadratic term induces a negligible increase of k_{off}^0 for the highest x_b measured. Together with the observation that the off-rates vs force curves are straight lines in semi-log plot (Fig. S18), this points to the fact that our data are well fitted by the Bell model using only two parameters. Another possibility to explain the correlation in Fig. 3B is the involvement of the curvature of the energy landscape, which predicts k_{off}^0 to scale linearly with $1/x_b^2$ (80); this trend is not convincingly observed for our data (Fig. S23D). Therefore, we cannot rule out that the error in fitting the slope in the k_{off} vs force plots leads to a correlated error in the intercept of the y-axis. Nevertheless, some classical and new results from the literature point also to such a negative correlation (81, 82). Further refinements of the present experiment, in particular for anchor point determination, stability of the setup, precision of jump detection, as well as the precision of force calibration, would certainly help to address this issue.

CONCLUSION

As a conclusion, the combination of AFS and J-DNA has a sufficient accuracy to characterize the force-induced dissociation of individual FKBP12-rapamycin-FRB and antigen-nanobodies complexes. We also illustrated how the method allows the comparison of individual bonds of same nature and their monitoring under repeated actuation. Therefore, combining AFS and J-DNA has the potential to both answer fundamental questions and open the way to systematic chemomechanical characterization of biomedically relevant interactions.

AUTHOR CONTRIBUTIONS

CG and LL designed the research. YJW and CV carried out experiments. AA, PC, MF, DK, TS, and CG contributed reagents. LV and FR contributed to the acquisition software and to the experimental setup. YJW, CV, FR, CG, and LL analyzed data.

YJW, CV, CG, and LL wrote the manuscript. All authors critically revised the manuscript.

DECLARATION OF INTEREST

PSL valorisation has submitted a patent related to the J-DNA (PCT FR2018/053533) with DK, TS, and CG among the inventors.

ACKNOWLEDGMENTS

We thank Lumicks (in particular Douwe Kamsma and Eugen Ostrofet), as well as Pierre-Henri Puech, Jean-François Allemand and Yan Jie for fruitful discussions. The AFS setup was acquired thanks to the grant Projet exploratoire région PACA 2017 – AcouLeuco obtained by FR. We thank AMIDEX Emergence Innovation (project ForSelecAntibody), Plan Cancer PhysCancer program (project ComPhysAb), European Research Council (ERC, grant agreement No. 772257), Human Frontier Science Program (HFSP, grant No. RGP0056/2018), PSL valorisation (project J-DNA), CNRS Defi Instrumentation aux Limites (project ForcaRapa), Marie Curie Skłodowska action (MSCA-IF, grant agreement 895819), and Labex Memolife (project Gephyrin). The Molecular Motors and Machines team at IBENS is an "Equipe labellisée" by the Ligue Nationale Contre le Cancer. We also acknowledge INSERM, CNRS, and AMU for regular support.

REFERENCES

1. Kim, J., C.-Z. Zhang, X. Zhang, and T. A. Springer, 2010. A Mechanically Stabilized Receptor–Ligand Flex-Bond Important in the Vasculature. *Nature* 466:992–995.
2. Gao, Y., S. Zorman, G. Gundersen, Z. Xi, L. Ma, G. Sirinakis, J. E. Rothman, and Y. Zhang, 2012. Single Reconstituted Neuronal SNARE Complexes Zipper in Three Distinct Stages. *Science* 337:1340–1343.
3. Huse, M., 2017. Mechanical Forces in the Immune System. *Nature Reviews Immunology* 17:679–690.
4. Rognoni, L., J. Stigler, B. Pelz, J. Ylanne, and M. Rief, 2012. Dynamic Force Sensing of Filamin Revealed in Single-Molecule Experiments. *Proceedings of the National Academy of Sciences* 109:19679–19684.
5. Limozin, L., and P.-H. Puech, 2019. Membrane Organization and Physical Regulation of Lymphocyte Antigen Receptors: A Biophysicist's Perspective. *The Journal of Membrane Biology* 252:397–412.
6. Schwesinger, F., R. Ros, T. Strunz, D. Anselmetti, H.-J. Guntherodt, A. Honegger, L. Jermutus, L. Tiefenauer, and A. Pluckthun, 2000. Unbinding Forces of Single Antibody-Antigen Complexes Correlate with Their Thermal Dissociation Rates. *Proceedings of the National Academy of Sciences* 97:9972–9977.

7. Rico, F., A. Russek, L. González, H. Grubmüller, and S. Scheuring, 2019. Heterogeneous and Rate-Dependent Streptavidin–Biotin Unbinding Revealed by High-Speed Force Spectroscopy and Atomistic Simulations. *Proceedings of the National Academy of Sciences* 116:6594–6601.
8. Kulin, S., R. Kishore, J. B. Hubbard, and K. Helmerson, 2002. Real-Time Measurement of Spontaneous Antigen-Antibody Dissociation. *Biophysical Journal* 83:1965–1973.
9. Merkel, R., P. Nassoy, A. Leung, K. Ritchie, and E. Evans, 1999. Energy Landscapes of Receptor–Ligand Bonds Explored with Dynamic Force Spectroscopy. *Nature* 397:50–53.
10. Dudko, O. K., G. Hummer, and A. Szabo, 2008. Theory, Analysis, and Interpretation of Single-Molecule Force Spectroscopy Experiments. *Proceedings of the National Academy of Sciences* 105:15755–15760.
11. Shang, H., and G. U. Lee, 2007. Magnetic Tweezers Measurement of the Bond Lifetime-Force Behavior of the IgG-Protein A Specific Molecular Interaction. *Journal of the American Chemical Society* 129:6640–6646.
12. Robert, P., K. Sengupta, P.-H. Puech, P. Bongrand, and L. Limozin, 2008. Tuning the Formation and Rupture of Single Ligand-Receptor Bonds by Hyaluronan-Induced Repulsion. *Biophysical Journal* 95:3999–4012.
13. Gonzalez, C., P. Chames, B. Kerfelec, D. Baty, P. Robert, and L. Limozin, 2019. Nanobody-CD16 Catch Bond Reveals NK Cell Mechanosensitivity. *Biophysical Journal* 116:1516–1526.
14. Halvorsen, K., and W. P. Wong, 2010. Massively Parallel Single-Molecule Manipulation Using Centrifugal Force. *Biophysical Journal* 98:L53–L55.
15. Yang, D., A. Ward, K. Halvorsen, and W. P. Wong, 2016. Multiplexed Single-Molecule Force Spectroscopy Using a Centrifuge. *Nature Communications* 7:11026.
16. Park, I. S., K. Eom, J. Son, W.-J. Chang, K. Park, T. Kwon, D. S. Yoon, R. Bashir, and S. W. Lee, 2012. Microfluidic Multifunctional Probe Array Dielectrophoretic Force Spectroscopy with Wide Loading Rates. *ACS Nano* 6:8665–8673.
17. Sitters, G., D. Kamsma, G. Thalhammer, M. Ritsch-Martel, E. J. G. Peterman, and G. J. L. Wuite, 2015. Acoustic Force Spectroscopy. *Nature Methods* 12:47–50.
18. Kamsma, D., R. Creyghton, G. Sitters, G. J. Wuite, and E. J. Peterman, 2016. Tuning the Music: Acoustic Force Spectroscopy (AFS) 2.0. *Methods* 105:26–33.
19. Hackl, M., E. V. Contrada, J. E. Ash, A. Kulkarni, J. Yoon, H.-Y. Cho, K.-B. Lee, J. M. Yarbrough, C. A. López, S. Gnanakaran, and S. P. S. Chundawat, 2022. Acoustic Force Spectroscopy Reveals Subtle Differences in Cellulose Unbinding Behavior of Carbohydrate-Binding Modules. *Proceedings of the National Academy of Sciences* 119:e2117467119.

20. Kostrz, D., H. K. Wayment-Steele, J. L. Wang, M. Follenfant, V. S. Pande, T. R. Strick, and C. Gosse, 2019. A Modular DNA Scaffold to Study Protein–Protein Interactions at Single-Molecule Resolution. *Nature Nanotechnology* 14:988–993.
21. Popa, I., J. A. Rivas-Pardo, E. C. Eckels, D. J. Echelman, C. L. Badilla, J. Valle-Orero, and J. M. Fernández, 2016. A HaloTag Anchored Ruler for Week-Long Studies of Protein Dynamics. *Journal of the American Chemical Society* 138:10546–10553.
22. Halvorsen, K., D. Schaak, and W. P. Wong, 2011. Nanoengineering a Single-Molecule Mechanical Switch Using DNA Self-Assembly. *Nanotechnology* 22:494005.
23. Gosse, C., T. R. Strick, and D. Kostrz, 2019. Molecular Scaffolds: When DNA Becomes the Hardware for Single-Molecule Investigations. *Current Opinion in Chemical Biology* 53:192–203.
24. Johnson, K. C., and W. E. Thomas, 2018. How Do We Know When Single-Molecule Force Spectroscopy Really Tests Single Bonds? *Biophysical Journal* 114:2032–2039.
25. Wang, Y., S. F. H. Barnett, S. Le, Z. Guo, X. Zhong, P. Kanchanawong, and J. Yan, 2019. Label-Free Single-Molecule Quantification of Rapamycin-induced FKBP–FRB Dimerization for Direct Control of Cellular Mechanotransduction. *Nano Letters* 19:7514–7525.
26. Bauer, M. S., S. Gruber, A. Hausch, P. S. F. C. Gomes, L. F. Milles, T. Nicolaus, L. C. Schendel, P. L. Navajas, E. Procko, D. Lietha, M. C. R. Melo, R. C. Bernardi, H. E. Gaub, and J. Lipfert, 2022. A Tethered Ligand Assay to Probe SARS-CoV-2:ACE2 Interactions. *Proceedings of the National Academy of Sciences* 119:e2114397119.
27. Kilchherr, F., C. Wachauf, B. Pelz, M. Rief, M. Zacharias, and H. Dietz, 2016. Single-Molecule Dissection of Stacking Forces in DNA. *Science* 353:aaf5508–aaf5508.
28. Shrestha, P., D. Yang, T. E. Tomov, J. I. MacDonald, A. Ward, H. T. Bergal, E. Krieg, S. Cabi, Y. Luo, B. Nathwani, A. Johnson-Buck, W. M. Shih, and W. P. Wong, 2021. Single-Molecule Mechanical Fingerprinting with DNA Nanoswitch Calipers. *Nature Nanotechnology* 16:1362–1370.
29. Mickolajczyk, K. J., P. D. B. Olinares, B. T. Chait, S. Liu, and T. M. Kapoor, 2022. The MIDAS Domain of AAA Mechanoenzyme Mdn1 Forms Catch Bonds with Two Different Substrates. *eLife* 11:e73534.
30. Penth, M., K. Schellhuber, R. Bennewitz, and J. Blass, 2021. Nanomechanics of Self-Assembled DNA Building Blocks. *Nanoscale* 13:9371–9380.
31. Li, N., J. Wang, K. Ma, L. Liang, L. Mi, W. Huang, X. Ma, Z. Wang, W. Zheng, L. Xu, J.-H. Chen, and Z. Yu, 2019. The Dynamics of Forming a Triplex in an Artificial Telomere Inferred by DNA Mechanics. *Nucleic Acids Research* 47:e86–e86.

32. Ma, X., M. Zhu, J. Liu, X. Li, L. Qu, L. Liang, W. Huang, J. Wang, N. Li, J.-H. Chen, W. Zhang, and Z. Yu, 2019. Interactions between PHD3-Bromo of MLL1 and H3K4me3 Revealed by Single-Molecule Magnetic Tweezers in a Parallel DNA Circuit. *Bioconjugate Chemistry* 30:2998–3006.
33. Maciuba, K., F. Zhang, and C. M. Kaiser, 2021. Facile Tethering of Stable and Unstable Proteins for Optical Tweezers Experiments. *Biophysical Journal* 120:2691–2700.
34. Mukhortava, A., and M. Schlierf, 2016. Efficient Formation of Site-Specific Protein–DNA Hybrids Using Copper-Free Click Chemistry. *Bioconjugate Chemistry* 27:1559–1563.
35. Synakewicz, M., D. Bauer, M. Rief, and L. S. Itzhaki, 2019. Bioorthogonal Protein–DNA Conjugation Methods for Force Spectroscopy. *Scientific Reports* 9:13820.
36. van der Sleen, L. M., and K. M. Tych, 2021. Bioconjugation Strategies for Connecting Proteins to DNA-Linkers for Single-Molecule Force-Based Experiments. *Nanomaterials* 11:2424.
37. Koussa, M. A., M. Sotomayor, and W. P. Wong, 2014. Protocol for Sortase-Mediated Construction of DNA–Protein Hybrids and Functional Nanostructures. *Methods* 67:134–141.
38. Madsen, M., and K. V. Gothelf, 2019. Chemistries for DNA Nanotechnology. *Chemical Reviews* 119:6384–6458.
39. Wang, J. L., C. Duboc, Q. Wu, T. Ochi, S. Liang, S. E. Tsutakawa, S. P. Lees-Miller, M. Nadal, J. A. Tainer, T. L. Blundell, and T. R. Strick, 2018. Dissection of DNA Double-Strand-Break Repair Using Novel Single-Molecule Forceps. *Nature Structural & Molecular Biology* 25:482–487.
40. Strick, T., J.-F. Allemand, D. Bensimon, A. Bensimon, and V. Croquette, 1996. The Elasticity of a Single Supercoiled DNA Molecule. *Science* 271:1835–1837.
41. Gosse, C., and V. Croquette, 2002. Magnetic Tweezers: Micromanipulation and Force Measurement at the Molecular Level. *Biophysical Journal* 82:3314–3329.
42. Klaue, D., and R. Seidel, 2009. Torsional Stiffness of Single Superparamagnetic Microspheres in an External Magnetic Field. *Physical Review Letters* 102:028302.
43. De Vlaminck, I., T. Henighan, M. T. J. van Loenhout, D. R. Burnham, and C. Dekker, 2012. Magnetic Forces and DNA Mechanics in Multiplexed Magnetic Tweezers. *PLoS ONE* 7:e41432.
44. Shon, M. J., S.-H. Rah, and T.-Y. Yoon, 2019. Submicrometer Elasticity of Double-Stranded DNA Revealed by Precision Force-Extension Measurements with Magnetic Tweezers. *Science Advances* 5:eaav1697.
45. Winkler, A., C. Richard, F. Oswald, D. Kamsma, S. Menzel, and T. Gemming, 2018. Performance Exploration of Acoustic Force Spectroscopy (AFSTM) Chips. *In Poster Presentation. Colloquium Acoustofluidics 2018. Lille.*

46. Nguyen, A., M. Brandt, T. M. Muenker, and T. Betz, 2021. Multi-Oscillation Microrheology *via* Acoustic Force Spectroscopy Enables Frequency-Dependent Measurements on Endothelial Cells at High-Throughput. *Lab on a Chip* 21:1929–1947.
47. Chen, J., X. F. Zheng, E. J. Brown, and S. L. Schreiber, 1995. Identification of an 11-kDa FKBP12-rapamycin-binding Domain within the 289-kDa FKBP12-rapamycin-associated Protein and Characterization of a Critical Serine Residue. *Proceedings of the National Academy of Sciences* 92:4947–4951.
48. Leone, M., K. J. Crowell, J. Chen, D. Jung, G. G. Chiang, S. Sareth, R. T. Abraham, and M. Pellecchia, 2006. The FRB Domain of mTOR: NMR Solution Structure and Inhibitor Design. *Biochemistry* 45:10294–10302.
49. Tao, Z., J. Barker, S. D.-H. Shi, M. Gehring, and S. Sun, 2010. Steady-State Kinetic and Inhibition Studies of the Mammalian Target of Rapamycin (mTOR) Kinase Domain and mTOR Complexes. *Biochemistry* 49:8488–8498.
50. Banaszynski, L. A., C. W. Liu, and T. J. Wandless, 2005. Characterization of the FKBP-Rapamycin-FRB Ternary Complex. *Journal of the American Chemical Society* 127:4715–4721.
51. Flaxman, H. A., C.-F. Chang, H.-Y. Wu, C. H. Nakamoto, and C. M. Woo, 2019. A Binding Site Hotspot Map of the FKBP12–Rapamycin–FRB Ternary Complex by Photoaffinity Labeling and Mass Spectrometry-Based Proteomics. *Journal of the American Chemical Society* 141:11759–11764.
52. Tamura, T., Y. Kioi, T. Miki, S. Tsukiji, and I. Hamachi, 2013. Fluorophore Labeling of Native FKBP12 by Ligand-Directed Tosyl Chemistry Allows Detection of Its Molecular Interactions *In Vitro* and in Living Cells. *Journal of the American Chemical Society* 135:6782–6785.
53. Lu, C., and Z.-X. Wang, 2017. Quantitative Analysis of Ligand Induced Heterodimerization of Two Distinct Receptors. *Analytical Chemistry* 89:6926–6930.
54. Choi, J., J. Chen, S. L. Schreiber, and J. Clardy, 1996. Structure of the FKBP12-Rapamycin Complex Interacting with Binding Domain of Human FRAP. *Science* 273:239–242.
55. Aylett, C. H. S., E. Sauer, S. Imseng, D. Boehringer, M. N. Hall, N. Ban, and T. Maier, 2016. Architecture of Human mTOR Complex 1. *Science* 351:48–52.
56. Joshi, D. C., C. Gosse, S.-Y. Huang, and J.-H. Lin, 2022. A Curvilinear-Path Umbrella Sampling Approach to Characterizing the Interactions Between Rapamycin and Three FKBP12 Variants. *Frontiers in Molecular Biosciences* 9:879000.
57. Martelli, A. M., F. Buontempo, and J. A. McCubrey, 2018. Drug Discovery Targeting the mTOR Pathway. *Clinical Science* 132:543–568.
58. Li, J., S. G. Kim, and J. Blenis, 2014. Rapamycin: One Drug, Many Effects. *Cell Metabolism* 19:373–379.

59. Chames, P., and U. Rothbauer, 2020. Special Issue: Nanobody. *Antibodies* 9:6.
60. Turini, M., P. Chames, P. Bruhns, D. Baty, and B. Kerfelec, 2014. A FcγRIII-engaging Bispecific Antibody Expands the Range of HER2-expressing Breast Tumors Eligible to Antibody Therapy. *Oncotarget* 5:5304–5319.
61. Bouchet, J., S. E. Basmaciogullari, P. Chrobak, B. Stolp, N. Bouchard, O. T. Fackler, P. Chames, P. Jolicoeur, S. Benichou, and D. Baty, 2011. Inhibition of the Nef Regulatory Protein of HIV-1 by a Single-Domain Antibody. *Blood* 117:3559–3568.
62. Chin, J. W., S. W. Santoro, A. B. Martin, D. S. King, L. Wang, and P. G. Schultz, 2002. Addition of P-Azido-L-phenylalanine to the Genetic Code of *E. Coli*. *Journal of the American Chemical Society* 124:9026–9027.
63. Young, T. S., I. Ahmad, J. A. Yin, and P. G. Schultz, 2010. An Enhanced System for Unnatural Amino Acid Mutagenesis in *E. Coli*. *Journal of Molecular Biology* 395:361–374.
64. Lajoie, M. J., A. J. Rovner, D. B. Goodman, H.-R. Aerni, A. D. Haimovich, G. Kuznetsov, J. A. Mercer, H. H. Wang, P. A. Carr, J. A. Mosberg, N. Rohland, P. G. Schultz, J. M. Jacobson, J. Rinehart, G. M. Church, and F. J. Isaacs, 2013. Genomically Recoded Organisms Expand Biological Functions. *Science* 342:357–360.
65. Nevoltris, D., B. Lombard, E. Dupuis, G. Mathis, P. Chames, and D. Baty, 2015. Conformational Nanobodies Reveal Tethered Epidermal Growth Factor Receptor Involved in EGFR/ErbB2 Predimers. *ACS Nano* 9:1388–1399.
66. Lin, C.-W., and A. Y. Ting, 2006. Transglutaminase-Catalyzed Site-Specific Conjugation of Small-Molecule Probes to Proteins in Vitro and on the Surface of Living Cells. *Journal of the American Chemical Society* 128:4542–4543.
67. Jeger, S., K. Zimmermann, A. Blanc, J. Grünberg, M. Honer, P. Hunziker, H. Struthers, and R. Schibli, 2010. Ortsspezifische und stöchiometrische Modifikation von Antikörpern durch bakterielle Transglutaminase. *Angewandte Chemie* 122:10191–10194.
68. Wong, W. P., and K. Halvorsen, 2006. The Effect of Integration Time on Fluctuation Measurements: Calibrating an Optical Trap in the Presence of Motion Blur. *Optics Express* 14:12517.
69. Daldrop, P., H. Brutzer, A. Huhle, D. J. Kauert, and R. Seidel, 2015. Extending the Range for Force Calibration in Magnetic Tweezers. *Biophysical Journal* 108:2550–2561.
70. Schäffer, E., S. F. Nørrelykke, and J. Howard, 2007. Surface Forces and Drag Coefficients of Microspheres near a Plane Surface Measured with Optical Tweezers. *Langmuir* 23:3654–3665.
71. Raible, M., M. Evstigneev, F. Bartels, R. Eckel, M. Nguyen-Duong, R. Merkel, R. Ros, D. Anselmetti, and P. Reimann, 2006. Theoretical Analysis of Single-Molecule Force Spectroscopy Experiments: Heterogeneity of Chemical Bonds. *Biophysical Journal* 90:3851–3864.

72. Lo Schiavo, V., P. Robert, L. Limozin, and P. Bongrand, 2012. Quantitative Modeling Assesses the Contribution of Bond Strengthening, Rebinding and Force Sharing to the Avidity of Biomolecule Interactions. *PLoS ONE* 7:e44070.
73. Xia, J., J. Zuo, and H. Li, 2022. Molecular Homogeneity of GB1 Revealed by Single Molecule Force Spectroscopy. *Nanoscale* 14:9925–9931.
74. Rico, F., and V. T. Moy, 2007. Energy Landscape Roughness of the Streptavidin–Biotin Interaction. *Journal of Molecular Recognition* 20:495–501.
75. Robert, P., A. Nicolas, S. Aranda-Espinoza, P. Bongrand, and L. Limozin, 2011. Minimal Encounter Time and Separation Determine Ligand-Receptor Binding in Cell Adhesion. *Biophysical Journal* 100:2642–2651.
76. Limozin, L., P. Bongrand, and P. Robert, 2016. A Rough Energy Landscape to Describe Surface-Linked Antibody and Antigen Bond Formation. *Scientific Reports* 6:35193.
77. Luo, Y., J. Chang, D. Yang, J. S. Bryan, M. MacIsaac, S. Pressé, and W. P. Wong, 2023. Resolving Molecular Heterogeneity with Single-Molecule Centrifugation. *Journal of the American Chemical Society* jacs.2c11450.
78. Walton, E. B., S. Lee, and K. J. Van Vliet, 2008. Extending Bell’s Model: How Force Transducer Stiffness Alters Measured Unbinding Forces and Kinetics of Molecular Complexes. *Biophysical Journal* 94:2621–2630.
79. Friddle, R. W., A. Noy, and J. J. De Yoreo, 2012. Interpreting the Widespread Nonlinear Force Spectra of Intermolecular Bonds. *Proceedings of the National Academy of Sciences* 109:13573–13578.
80. Hummer, G., and A. Szabo, 2003. Kinetics from Nonequilibrium Single-Molecule Pulling Experiments. *Biophysical Journal* 85:5–15.
81. Evans, E. A., and D. A. Calderwood, 2007. Forces and Bond Dynamics in Cell Adhesion. *Science* 316:1148–1153.
82. Pettmann, J., L. Awada, B. Rózycki, A. Huhn, S. Faour, M. Kutuzov, L. Limozin, T. R. Weikl, P. A. van der Merwe, P. Robert, and O. Dushek, 2022. Mechanical Forces Impair Antigen Discrimination by Reducing Differences in T-cell Receptor/Peptide–MHC Off-rates. *The EMBO Journal* .